

Zero-Shot Statistical Downscaling via Diffusion Posterior Sampling

Ruiyan Tie ^{* 1 2 3} Wenbo Xiong ^{* 4 2 3} Zhengyu Shi ^{* 1 3} Xinyu Su ^{1 3} Chenyu Jiang ^{4 3} Libo Wu ^{† 5 2 3} Hao Li ^{† 1 2 3}

Abstract

Conventional supervised climate downscaling struggles to generalize to Global Climate Models (GCMs) due to the lack of paired training data and inherent domain gaps relative to reanalysis. Meanwhile, current zero-shot methods suffer from physical inconsistencies and vanishing gradient issues under large scaling factors. We propose Zero-Shot Statistical Downscaling (ZSSD), a zero-shot framework that performs statistical downscaling without paired data during training. ZSSD leverages a Physics-Consistent Climate Prior learned from reanalysis data, conditioned on geophysical boundaries and temporal information to enforce physical validity. Furthermore, to enable robust inference across varying GCMs, we introduce Unified Coordinate Guidance. This strategy addresses the vanishing gradient problem in vanilla DPS and ensures consistency with large-scale fields. Results show that ZSSD significantly outperforms existing zero-shot baselines in 99th percentile errors and successfully reconstructs complex weather events, such as tropical cyclones, across heterogeneous GCMs.

1. Introduction

Climate downscaling refers to the process of translating coarse-resolution climate data into high-resolution representations (Hewitson & Crane, 1996), and is commonly applied to the outputs of Global Climate Models (GCMs) (Meehl et al., 2000). By recovering fine-resolution atmospheric details that are smoothed out in global simulations, downscaling enables the characterization of extreme weather events, such as tropical cyclones (Calvin et al., 2023), that cannot be

^{*} Equal contribution. [†] Corresponding author. ¹Artificial Intelligence Innovation and Incubation Institute, Fudan University, Shanghai, China ²Shanghai Innovation Institute, Shanghai, China ³Shanghai Academy of AI for Science, Shanghai, China ⁴School of Data Science, Fudan University, Shanghai, China ⁵Institution for Big Data, Fudan University, Shanghai, China. Correspondence to: Libo Wu <wulibo@fudan.edu.cn>, Hao Li <li-hao.lh@fudan.edu.cn>.

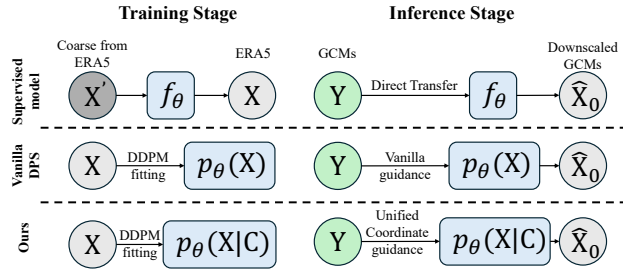


Figure 1. Schematic comparison of different downscaling paradigms. (Top) Supervised models learn a deterministic mapping f_θ from coarse (X') to high-resolution (X) ERA5 data. (Middle) Vanilla DPS utilizes an unconditional diffusion prior $p_\theta(X)$ with standard guidance. (Bottom) **Ours** (ZSSD) introduces a conditioned Physics-Consistent Climate Prior $p_\theta(X|C)$ and employs Unified Coordinate Guidance during inference. C denotes boundary conditions and temporal information.

resolved at coarse resolution and are important for disaster preparedness and risk mitigation (O’Neill et al., 2016).

Deep learning-based statistical downscaling, which learns the coarse-to-fine mapping, has advanced significantly. However, applying standard supervised learning to climate downscaling is difficult due to the simulation mechanisms of GCMs. GCMs simulate a parallel Earth governed by the same physics as the real climate system, but their internal weather evolution follows an independent timeline. As a result, weather events simulated on a given model date do not correspond to the actual historical events observed on that date. This inherent temporal mismatch leads to unpaired training samples, undermining the strict input–output correspondence assumed by conventional supervised learning frameworks (Li et al., 2025; Tie et al., 2025; Schmidt et al., 2025). When such mismatched data are naively forced into a supervised mapping, commonly used regression objectives tend to favor conditional mean solutions, resulting in over-smoothed outputs that underestimate realistic variability. Alternatively, models trained on paired ERA5 data can be directly transferred to GCMs, yet they suffer from significant domain gaps (Fig. 1, top).

To alleviate the limitations of such paired training between GCMs simulations and real meteorological observations, insights from recent advances in low-level vision inverse problems suggest that diffusion priors can be effective for

reconstruction in a zero-shot (i.e., unpaired) manner. Recent work (Schmidt et al., 2025) adopts Diffusion Posterior Sampling (DPS) for unpaired climate downscaling by guiding the sampling process of a pre-trained unconditional diffusion model with low-quality observations to recover high-resolution physics-consistent details. Their results demonstrate the feasibility of leveraging generative priors to bridge the domain gap between simulations and observations without explicit supervision.

However, the vanilla DPS faces inherent limitations due to its reliance on an unconditional prior, which often struggles to capture physically consistent atmospheric distribution structures, resulting in predictions that may lack physical consistency. Furthermore, in downscaling tasks with large scaling factors, the guidance signal requires calculating gradients through a highly compressive degradation operator. This process induces a severe vanishing gradient problem, rendering the coarse input ineffective in steering the generation trajectory. Consequently, the outputs frequently exhibit severe systematic biases.

To address the limitations of vanilla DPS in global climate downscaling, we introduce **Zero-Shot Statistical Downscaling** (ZSSD), which does not require low-resolution GCMs data during the training stage, comparison is illustrated in Fig. 1. ZSSD combines (i) a Physics-Consistent Climate Prior, which explicitly models intrinsic atmospheric dynamics to rectify the structural deficiencies of vanilla priors; and (ii) a Unified Coordinate Guidance mechanism, which effectively mitigates the domain gap and vanishing gradient problem under large scaling factors (e.g., 20 \times). Specifically, the Physics-Consistent Climate Prior incorporates geophysical boundaries (e.g., topography) and temporal embeddings (e.g., season, time of day) as conditions. This design ensures the model learns intrinsic atmospheric physics, thereby capturing realistic spatial structures. The Unified Coordinate Guidance first downsamples inputs to a unified coarse scale (5°) to retain reliable large-scale circulation patterns. Instead of computing gradients on the coarse grid as in previous work, we re-project the data back onto the unified high-resolution coordinate system (0.25°) using interpolation. By mapping the coarse constraint into the high-resolution space, this strategy stabilizes the effective guidance, ensuring input information is preserved during sampling. In summary, our main contributions are as follows:

- We propose ZSSD, a framework for simultaneous downscaling and quantile bias correction that leverages coarse inputs from arbitrary GCMs.
- We construct a Physics-Consistent Climate Diffusion Prior that conditions on static boundary constraints to ensure physically valid generation.

- We introduce Unified Coordinate Guidance to address the vanishing gradient problem in vanilla DPS. By computing gradients in the high-resolution space while preserving trustworthy large-scale components, this strategy ensures robust structural recovery under large scaling factors.
- In terms of 99th percentile error, ZSSD matches supervised baselines on paired tasks and achieves state-of-the-art (SOTA) performance on unpaired benchmarks.

2. Related Work

Unpaired Learning for Climate Downscaling. Supervised methods require paired data, but GCM simulations and real-world observations are inherently unpaired. To address this mismatch, researchers have turned to zero-shot learning. Groenke et al. (2020) first used Normalizing Flows to align the statistical distributions of coarse simulations and high-resolution observations. Li et al. (2025) later proposed a CycleGAN-based approach that learns to translate between the two domains without needing paired examples. Most recently, Schmidt et al. (2025) treated downscaling as a Bayesian inverse problem by adopting a vanilla DPS approach. They used a pre-trained score model as a prior and guided the generation process with raw coarse inputs, ensuring the output was consistent with the coarse inputs. However, these methods have two main limitations. First, the standard prior lacks physical consistency, which can lead to predictions that violate physical laws. Second, vanilla DPS suffers from the vanishing gradient problem when the scaling factor is large. This makes the guidance ineffective and leads to severe biases in the results.

Solving Inverse Problems via Diffusion Priors. Leveraging diffusion models as priors for inverse problems has evolved from exploiting operator linearity to handling general non-linear degradations. For linear tasks, Kawar et al. (2022) and Wang et al. (2022) proposed DDRM and DDNM, respectively, which utilize SVD or Null-space decomposition to analytically enforce spectral consistency. To extend applicability to general operators where such decomposition is infeasible, building upon the gradient guidance strategy in (Chung et al., 2022b), Chung et al. (2022a) introduced DPS, which approximates the likelihood score to guide the reverse process. Addressing the high computational cost of such gradient-based guidance, recent approaches focused on acceleration strategies (Zhu et al., 2023) or variational formulations (Mardani et al., 2023) that optimize the evidence lower bound directly for improved theoretical rigor.

3. Preliminaries

Climate Downscaling. Let $\mathbf{Y} \in \mathbb{R}^{h \times w \times C}$ denote a coarse-resolution atmospheric state at a given time, where h and w represent the spatial grid dimensions (latitude and lon-

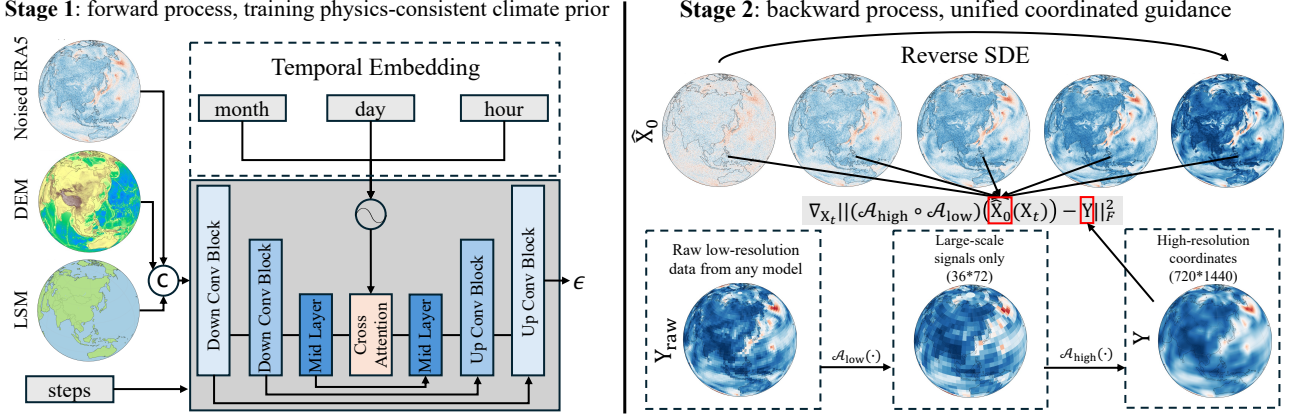


Figure 2. Overview of the ZSSD framework. The method consists of two stages. Left (Stage 1): We train a diffusion prior on ERA5 data conditioned on static terrain (DEM, LSM) and cyclic time embeddings (month, day, hour). Right (Stage 2): During inference (Reverse Stochastic Differential Equation, Reverse SDE), we employ unified coordinate guidance. The raw input \mathbf{Y}_{raw} is first processed by $\mathcal{A}_{\text{low}}(\cdot)$ to isolate reliable large-scale components, and subsequently interpolated to the unified high-resolution coordinate system via $\mathcal{A}_{\text{high}}(\cdot)$. Crucially, the estimated clean state $\hat{\mathbf{X}}_0$ undergoes this identical transformation pipeline. The guidance signal is then obtained by computing the gradient of the distance between these two aligned representations with respect to \mathbf{X}_t .

tude), and C denotes the number of physical variables (e.g., wind components and pressure). The corresponding high-resolution atmospheric state is denoted as $\mathbf{X} \in \mathbb{R}^{H \times W \times C}$, defined on a finer spatial grid, with $h \ll H$ and $w \ll W$. Climate downscaling aims to recover fine-scale atmospheric states from coarse-resolution simulations. Although here \mathbf{X} and \mathbf{Y} are three-dimensional tensors, we represent them as two-dimensional matrices for notational simplicity in the following text, without loss of generality.

We formulate task as an ill-posed inverse problem, where the coarse-resolution field \mathbf{Y} is degraded from the latent high-resolution state \mathbf{X} through a non-invertible measurement operator:

$$\mathbf{Y} = \mathcal{A}(\mathbf{X}) + \mathbf{N}, \quad (1)$$

where $\mathcal{A} : \mathbb{R}^{H \times W} \rightarrow \mathbb{R}^{h \times w}$ models spatial aggregation and resolution transform, and $\mathbf{N} \sim \mathcal{MN}_{h \times w}(\mathbf{0}, \Sigma_h, \Sigma_w)$ accounts for measurement noise obeying a matrix variate Gaussian (MVG) distribution, Σ_h and Σ_w represent the row (latitudinal) and column (longitudinal) covariance matrices, respectively.

The objective is to learn a model f_θ that, given \mathbf{Y} , produces a high-resolution reconstruction $\hat{\mathbf{X}}$ consistent with the underlying fine-scale structures of \mathbf{X} , rather than merely increasing spatial resolution through interpolation.

Zero-Shot Climate Downscaling. This task aims to recover a high-resolution atmospheric state \mathbf{X} from a coarse-resolution observation \mathbf{Y} without assuming access to paired coarse- and high-resolution samples. The ill-posed nature of the inverse problem motivates a probabilistic formula-

tion, in which the solution is represented by the posterior distribution $p(\mathbf{X}|\mathbf{Y})$ rather than by a point estimate. Based on Bayes' rule, the posterior $p(\mathbf{X}|\mathbf{Y})$ can be formulated as shown in Eq. (2). Here, $p(\mathbf{X})$ denotes a prior distribution over physically and statistically plausible high-resolution atmospheric states, and likelihood $p(\mathbf{Y}|\mathbf{X})$ encodes the consistency between the reconstructed field and the observed coarse-resolution input. In this zero-shot setting, the prior and the low-resolution observation GCMs are specified independently, without relying on paired supervision.

$$p(\mathbf{X}|\mathbf{Y}) \propto \underbrace{p(\mathbf{Y}|\mathbf{X})}_{\text{Data Consistency}} \cdot \underbrace{p(\mathbf{X})}_{\text{Climate Prior}}. \quad (2)$$

4. Methodology

We present ZSSD, a zero-shot generative framework for statistical downscaling, which operates in two stages, as illustrated in Fig. 2. First, a Physics-Consistent Climate Prior is learned to capture universal spatial statistics of high-resolution atmospheric fields, thereby modeling the prior term (Section 4.1). Second, a Unified Coordinate Guidance mechanism is introduced to enable robust posterior sampling by enforcing consistency with the coarse-resolution input through the likelihood term (Section 4.2).

4.1. Physics-Consistent Climate Prior

In contrast to vanilla DPS formulations that employ an unconditional diffusion prior, we parameterize the prior using a conditional Denoising Diffusion Probabilistic Model (DDPM) (Ho et al., 2020), enabling the incorporation of physical constraints into the generative process.

In our specific setting, \mathbf{X}_0 represents the high-resolution atmospheric state variables sampled from reanalysis data. The conditional context \mathbf{C} constrains the solution space to physically plausible atmospheric states, thereby regularizing the generative process and reducing spurious artifacts. In our model, the conditional context \mathbf{C} integrates two complementary forms of physical prior information: static spatial boundaries and cyclic temporal information. Specifically, static spatial boundaries, denoted as S , including LSM and DEM, are incorporated via channel-wise concatenation to constrain the spatial structure of generated fields. In addition, cyclic temporal information, denoted as T , such as month, day, and hour, is encoded using sine-cosine positional embeddings and injected through cross-attention layers to capture seasonal and diurnal variability.

We adopt the standard formulation in DDPM. The forward process diffuses the data distribution into Gaussian noise, while the reverse process learns to recover the data. The forward marginal distribution $q(\mathbf{X}_t | \mathbf{X}_0)$ and the reverse transition $p_\theta(\mathbf{X}_{t-1} | \mathbf{X}_t, \mathbf{C})$ are parameterized as

$$\begin{aligned} q(\mathbf{X}_t | \mathbf{X}_0) &= \mathcal{N}(\mathbf{X}_t; \sqrt{\bar{\alpha}_t} \mathbf{X}_0, (1 - \bar{\alpha}_t) \mathbf{I}), \\ p_\theta(\mathbf{X}_{t-1} | \mathbf{X}_t, \mathbf{C}) &= \mathcal{N}(\mathbf{X}_{t-1}; \boldsymbol{\mu}_\theta(\mathbf{X}_t, t, \mathbf{C}), \beta_t \mathbf{I}), \end{aligned} \quad (3)$$

where β_t represents the pre-defined noise variance schedule, $\alpha_t \triangleq 1 - \beta_t$, $\bar{\alpha}_t \triangleq \prod_{s=1}^t \alpha_s$. $\boldsymbol{\mu}_\theta$ denotes the reverse process mean function approximator and $\boldsymbol{\mu}_\theta(\mathbf{X}_t, t, \mathbf{C}) = \frac{1}{\sqrt{\alpha_t}} (\mathbf{X}_t - \frac{\beta_t}{\sqrt{1 - \bar{\alpha}_t}} \boldsymbol{\epsilon}_\theta(\mathbf{X}_t, t, \mathbf{C}))$. The network $\boldsymbol{\epsilon}_\theta$ is trained to approximate the Gaussian noise $\boldsymbol{\epsilon}$ added during the forward process by minimizing the variational lower bound:

$$\mathcal{L} = \mathbb{E}_{\mathbf{X}_0, \boldsymbol{\epsilon}, t, \mathbf{C}} [\|\boldsymbol{\epsilon} - \boldsymbol{\epsilon}_\theta(\mathbf{X}_t, t, \mathbf{C})\|_F^2]. \quad (4)$$

4.2. Unified Coordinate Guidance DPS

As illustrated in Stage 2 of Fig. 2, to handle the diverse grid definitions across GCMs, we propose a Unified Coordinate Guidance strategy that transforms the raw input \mathbf{Y}_{raw} into the final guidance data \mathbf{Y} . Specifically, this process involves projecting \mathbf{Y}_{raw} into a unified low-resolution coordinate system using \mathcal{A}_{low} and subsequently re-projecting it back to the target high-resolution system to obtain \mathbf{Y} using $\mathcal{A}_{\text{high}}$, formulating the composite operator as $\mathbf{Y} = \mathcal{A}(\mathbf{Y}_{\text{raw}})$ and $\mathcal{A} = \mathcal{A}_{\text{high}} \circ \mathcal{A}_{\text{low}}$. Although this operation superficially resembles a filtering process, the underlying motivation is non-trivial.

First, inspired by Hess et al. (2025), we investigate the distributional discrepancies between the ERA5 and GCMs. By projecting these datasets into a 2D space using t-SNE, we observe distinct clustering phenomena among different models, as shown in Section 5.4. This empirical evidence confirms a significant domain gap, indicating that the ERA5 prior has limited generalization when directly applied to

Algorithm 1 Unified Coordinate Guidance Sampling

```

1: Input: Raw low-resolution  $\mathbf{Y}_{\text{raw}}$ , Condition  $\mathbf{C}$ , Steps  $T$ , Scale  $\zeta$ , Lat-Weights  $\mathbf{W}$ 
2: Define:  $\mathcal{A}_{\text{low}}(\cdot)$  and  $\mathcal{A}_{\text{high}}(\cdot)$ ,  $\sigma_t \triangleq \sqrt{\beta_t}$ 
3: Initialize:  $\mathbf{X}_T \sim \mathcal{N}(\mathbf{0}, \mathbf{I})$ ,  $\mathbf{Y} \leftarrow (\mathcal{A}_{\text{high}} \circ \mathcal{A}_{\text{low}})(\mathbf{Y}_{\text{raw}})$ 
4: for  $t = T - 1$  to 0 do
5:    $\mathbf{Z} \sim \mathcal{N}(\mathbf{0}, \mathbf{I})$ 
6:   Predict noise component  $\boldsymbol{\epsilon} \leftarrow \boldsymbol{\epsilon}_\theta(\mathbf{X}_t, t, \mathbf{C})$ 
7:   Estimate clean data  $\hat{\mathbf{X}}_0 \leftarrow \frac{1}{\sqrt{\bar{\alpha}_t}} (\mathbf{X}_t - \sqrt{1 - \bar{\alpha}_t} \boldsymbol{\epsilon})$ 
8:   Compute latitude-weighted gradient
     $\mathbf{G} \leftarrow \nabla_{\mathbf{x}_t} \|\mathbf{W}((\mathcal{A}_{\text{high}} \circ \mathcal{A}_{\text{low}})(\hat{\mathbf{X}}_0(\mathbf{X}_t, \mathbf{C})) - \mathbf{Y})\|_F^2$ 
9:   Compute mean  $\boldsymbol{\mu}_t \leftarrow \frac{1}{\sqrt{\alpha_t}} \left( \mathbf{X}_t - \frac{\beta_t}{\sqrt{1 - \bar{\alpha}_t}} \boldsymbol{\epsilon} \right)$ 
10:  Update state  $\mathbf{X}_{t-1} \leftarrow \boldsymbol{\mu}_t + \sigma_t \mathbf{Z} - \zeta \mathbf{G}$ 
11: end for
12: return  $\hat{\mathbf{X}}_0$ 

```

various GCMs. Consequently, directly using raw GCMs data as guidance (i.e., $\mathbf{Y} = \mathbf{Y}_{\text{raw}}$) introduces a domain gap that leads to model failure. To address this, we employ \mathcal{A}_{low} to filter out out-of-distribution (OOD) high-frequency components, ensuring the guidance signal remains within the prior's valid support to prevent mode collapse. Specifically, \mathcal{A}_{low} acts as a conservative downsampling function that maps dense fields to a fixed coarse scale (e.g., 5° resolution, 36×72 grid points). By computing the area-weighted average of pixels within each coarse cell, this operator ensures that mass and energy fluxes are conserved during the degradation process.

However, we observe that performing calculations directly on the extremely coarse output of \mathcal{A}_{low} leads to vanishing gradient. To address this, we define the universal measurement operator $\mathcal{A}_{\text{high}}$ as a unified upsampling function that maps the coarse scale back to the target resolution (e.g., 0.25° resolution, 720×1440 grid points). This design effectively unlocks the model's capability to perform downscaling with large scaling factors. Note that, $\mathcal{A}_{\text{high}}$ and \mathcal{A}_{low} therein are designed to accept inputs of arbitrary dimensions, while their output shapes are fixed at 720×1440 and 36×72 , respectively.

As aforementioned, the common measurement model is stated as $\mathbf{Y} = \mathcal{A}(\mathbf{X}_0) + \mathbf{N}$ and $\mathbf{N} \sim \mathcal{MN}_{H \times W}(\mathbf{0}, \boldsymbol{\Sigma}_H, \boldsymbol{\Sigma}_W)$. In our framework, $\boldsymbol{\Sigma}_W$ is set to \mathbf{I} by assuming longitudinal homoscedasticity, as the longitudinal span of grid cells remains invariant across the domain. Therefore, the log-likelihood is as follows:

$$\log p(\mathbf{Y} | \hat{\mathbf{X}}_0(\mathbf{X}_t, \mathbf{C})) \simeq -\|\mathbf{Y} - \mathcal{A}(\hat{\mathbf{X}}_0(\mathbf{X}_t, \mathbf{C}))\|_{\mathbf{A}, \mathbf{I}}^2, \quad (5)$$

where $\mathbf{A} \triangleq \boldsymbol{\Sigma}_H^{-1}$, $\|\mathbf{X}\|_{\mathbf{A}, \mathbf{I}}^2 \triangleq \text{Tr}(\mathbf{A} \mathbf{X} \mathbf{X}^\top)$, and $\hat{\mathbf{X}}_0$ is posterior mean as provided in Appendix A.1. The formulation of

Table 1. Summary of GCMs of CMIP6 used in this study.

MODEL NAME	INSTITUTION	NOM. RES.	GRID SIZE
IPSL-CM6A-LR	IPSL	~250 KM	144 × 143
AWI-ESM-1-1-LR	AWI	~250 KM	192 × 96
MPI-ESM1-2-LR	MPI-M	~250 KM	192 × 96
MIROC6	JAMSTEC	~140 KM	256 × 128
MPI-ESM1-2-HR	MPI-M	~100 KM	384 × 192

the above is derived from the density function for the MVG distribution (Gupta & Nagar, 1999).

Then, we rewrite the log-likelihood in Eq. (5) to quantify the distance between $\mathcal{A}(\hat{\mathbf{X}}_0)$ and \mathbf{Y} . We also incorporate latitude weighting into this distance calculation:

$$\mathcal{E}(\mathbf{X}_t, \mathbf{Y}) = \|\mathbf{W}(\mathcal{A}(\hat{\mathbf{X}}_0(\mathbf{X}_t, \mathbf{C})) - \mathbf{Y})\|_F^2, \quad (6)$$

where $\mathbf{W}^\top \mathbf{W} = \Sigma_H^{-1}$. Notably, the distance in Eq. (6) differs from the log-likelihood in Eq. (5) by only one negative sign. The weighting matrix \mathbf{W} combines the spherical geometry of the Earth and the measurement noise at different latitudes, with weights expressed as $\mathbf{W}_{ii} = \sqrt{\Sigma_{H_{ii}}^{-1}} \propto \cos(\phi_i)$, where ϕ_i is the latitude of the i -th grid row.

We use the gradient $\nabla_{\mathbf{x}_t} \mathcal{E}$ to guide the generation process. This ensures that the generated high-resolution data is consistent with the low-resolution input. Specifically, when downsampled back to the coarse scale, the generated output matches the original GCMs projection while preserving fine-scale variability. This approach preserves the fidelity of large-scale structures while augmenting realistic local details. The full process is shown in Algorithm 1. Additional methodological details can be found in Appendix A.1.

5. Experiments

5.1. Experimental Setup

Datasets. ERA5. We utilize the ERA5 reanalysis dataset (Hersbach et al., 2023) as our high-resolution ground truth, using its native 0.25° spatial resolution (720×1440 grid points) and subsampling it to 6-hour intervals. To provide a clear and challenging evaluation of downscaling performance, we focus on tropical cyclones-related atmospheric fields as a representative case. Specifically, we select five variables: Mean Sea Level Pressure (MSL) and 10 m Wind Components (U10M, V10M) to characterize near-surface intensity, and Geopotential Height at 500hPa and 250hPa (Z500, Z250) to represent upper-level circulation patterns.

GCMs Simulations in CMIP6. To evaluate the zero-shot generalization capability of our framework, we use 6-hourly outputs from the historical experiment of five different GCMs models in Coupled Model Intercomparison

Project Phase 6 (CMIP6) (Eyring et al., 2016), including IPSL-CM6A-LR (Boucher et al., 2020), AWI-ESM-1-1-LR (Semmler et al., 2020), MIROC6 (Tatebe et al., 2019), MPI-ESM1-2-LR and MPI-ESM1-2-HR (Mauritsen et al., 2019). As shown in Table 1, these models cover a range of resolutions from about 250 km to 100 km. This diversity enables an assessment of whether our method generalizes across different grid resolutions without model-specific retraining. We select the same variables as in the ERA5 dataset. In CMIP6, these are named ‘psl’ (MSL), ‘uas’ and ‘vas’ (10m wind), and ‘zg’ (geopotential height). Specifically, we multiply the ‘zg’ fields at 500hPa and 250hPa by the gravitational acceleration g to convert them into geopotential (Z), ensuring consistency with the ERA5 format.

The prior trained on ERA5 (1980–1999), validate on 2000, and test on 2001–2009 using both ERA5 and GCMs. GCMs data are not used in training or validation.

GENCO. We also incorporate topographic data from the Global Elevation and Continental-scale Ocean Bathymetry (GENCO), a high-resolution global digital elevation dataset (Mayer et al., 2018). The original 30m GENCO data are resampled to 0.25° resolution for this study, this topographic field is used as a static conditioning input in the generative prior.

Baselines. We categorize comparative models into three classes to establish performance benchmarks. First, traditional statistical downscaling methods, such as Bilinear interpolation and BCSD (Wood et al., 2002), serve as the fundamental performance baseline. Second, supervised deep learning methods, including SwinIR (Liang et al., 2021), ESRGAN (Wang et al., 2018), and CorDiff (Mardani et al., 2025), represent the SOTA performance for regression-based, GAN-based, and diffusion-based paradigms on paired tasks, respectively. Finally, we include DDRM (Kawar et al., 2022) and DPS (Chung et al., 2022a; Schmidt et al., 2025), representative diffusion-based inverse problem solvers, to assess the advantages of ZSSD without paired supervision.

Implementation Details. The backbone of our pre-trained prior is a 2D U-Net architecture with a four-level encoder–decoder structure and skip connections to preserve multi-scale spatial information. The channel dimensions for the downsampling and upsampling paths are set to $\{64, 128, 256, 512\}$, respectively. Crucially, the bottleneck stage incorporates cross-attention mechanisms to explicitly integrate temporal embeddings, conditioning the spatial features on time information. Each resolution level comprises two stacked residual blocks to enhance feature extraction capabilities.

The model was trained and inferred on a cluster of 8 NVIDIA H200 GPUs (141 GB memory per GPU). We used

Table 2. Quantitative comparison of downscaling methods on both paired (synthetic) and unpaired (GCMs) tasks. The values represent the spatial MAE/RMSE averaged over the test period (2001-2009). **Paired task** evaluates reconstruction from synthetic downsampling ($\times 6, \times 10, \times 20$), while **unpaired task** assesses zero-shot generalization across heterogeneous GCMs. Best results are highlighted in **bold** and underline denotes the second-best. Note that the output scale of \mathcal{A}_{low} adapts to the input resolution in paired tasks, whereas it is fixed at 5.0° in unpaired settings.

METHOD	PAIRED TASK (SYNTHETIC)			UNPAIRED TASK (REAL GCMs)				
	$1.5^\circ (\times 6)$	$2.5^\circ (\times 10)$	$5.0^\circ (\times 20)$	IPSL	MIROC6	AWI	MPI-LR	MPI-HR
BILINEAR	0.41 / 0.76	0.72 / 1.15	1.40 / 1.90	1.06 / 1.78	1.84 / 2.43	1.50 / 2.19	1.48 / 2.12	1.32 / 1.90
BCSD	0.40 / 0.75	0.70 / 1.13	1.35 / 1.83	<u>0.98 / 1.67</u>	<u>1.72 / 2.33</u>	<u>1.36 / 2.07</u>	<u>1.35 / 1.98</u>	<u>1.24 / 1.76</u>
DDRM	0.15 / 0.20	0.27 / 0.43	0.51 / 0.78	1.04 / 1.69	1.84 / 2.45	1.53 / 2.20	1.43 / 2.10	1.33 / 2.02
DPS	0.15 / 0.21	0.23 / 0.38	3.31 / 4.77	1.03 / <u>1.67</u>	1.84 / 2.40	1.48 / 2.13	1.40 / 2.08	1.32 / 1.89
ZSSD (OURS)	0.09 / 0.16	0.15 / 0.29	0.28 / 0.53	0.87 / 1.32	1.08 / 1.42	1.28 / 1.89	1.24 / 1.81	1.05 / 1.49

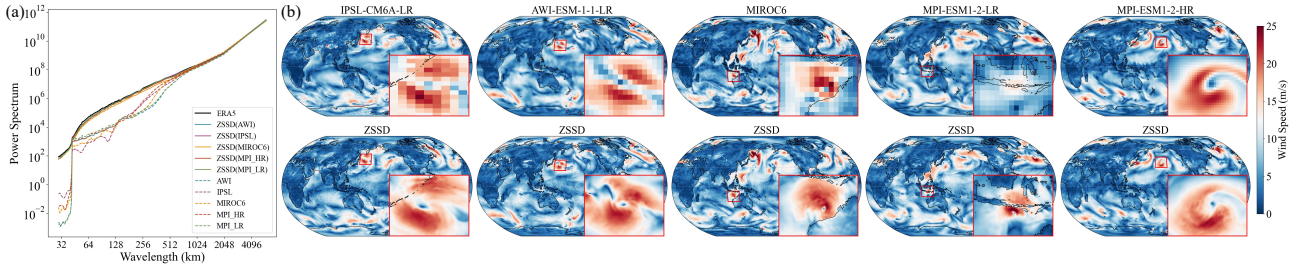


Figure 3. Spectral and spatial demonstration of ZSSD capabilities. **(a)** Annual mean power spectra of 10m Wind Speed (WS10m). **(b)** Visual comparison of WS10m and Tropical Cyclones. The **top row** displays raw outputs from various GCMs. The **bottom row** shows the corresponding high-resolution fields reconstructed by our ZSSD framework, revealing detailed vortex structures. Columns correspond to samples from (left to right): 2001-02-24 00:00, 2002-01-26 00:00, 2001-01-01 00:00, 2001-01-03 00:00, and 2001-03-16 00:00.

the AdamW optimizer with an initial learning rate of 10^{-4} . A StepLR scheduler with decays factor $\gamma = 0.9$ was applied every 100 epochs. Training was conducted for 300 epochs.

Evaluation Methods. Climate downscaling differs from short-term weather prediction in evaluation method. Although GCMs and ERA5 reanalysis share nominal timestamps in the historical period, their internal weather realizations are not phase-aligned, rendering pointwise time-synchronous comparison statistically inappropriate. Consequently, evaluation focuses on distributional consistency and extreme-state characteristics under comparable climatological conditions.

To evaluate the model’s ability to reproduce extreme climate states, we analyze the spatial statistics of upper-tail behavior. Specifically, the 99th percentile of each variable is computed over the test period (2001-2009) for both ERA5 and the downscale outputs. Discrepancies between the predicted extremes and the ERA5 reference are quantified using latitude-weighted Mean Absolute Error (MAE) and Root Mean Square Error (RMSE), defined in Appendix A.2. To reduce the impact of randomness, we calculate the average over 5 ensemble members.

5.2. Main Results

We demonstrate the effectiveness of our method across two distinct tasks. The first is a paired task, in which reconstruction performance is assessed using ERA5 data, with low-resolution inputs generated by synthetically downsampling the high-resolution reference. The second is a more challenging unpaired task, where ZSSD is directly applied to heterogeneous GCMs.

Overall Performance. Table 2 shows the comparison results. Our method (ZSSD) performs better than both traditional methods (Bilinear, BCSD) and other zero-shot diffusion methods (DDRM, DPS) in all tests.

On the paired task (synthetic data), ZSSD achieves the lowest errors. The advantage is most obvious at the largest scaling factor ($20\times$, or 5.0°). In this difficult setting, ZSSD keeps the MAE low at 0.28, while the vanilla DPS method fails with a very high error of 3.31. This proves that our “Unified Coordinate Guidance” works well and solves the gradient problem that affects other methods.

In the unpaired task (real GCMs), the advantage of ZSSD becomes even more pronounced. In this setting, supervised models are inapplicable due to the absence of paired training data and the heterogeneous resolutions and grid structures of GCMs. Conversely, ZSSD achieves SOTA results across all

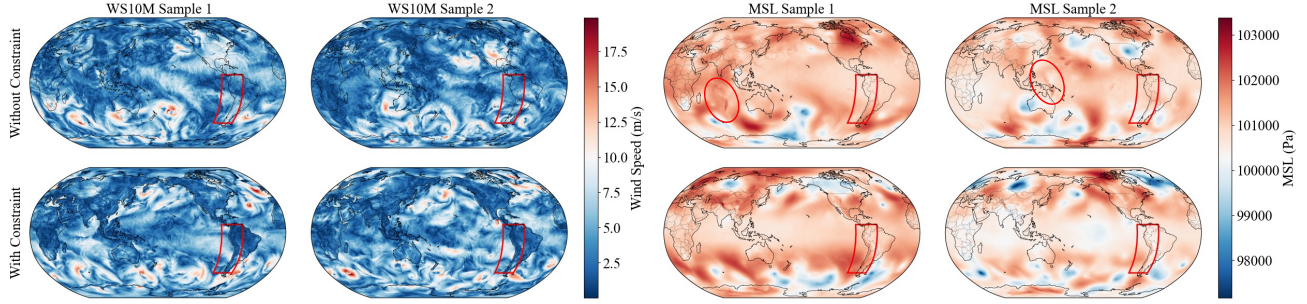


Figure 4. Impact of conditions on generated climate states. The Top Row (without constraints) lacks the physical terrain blocking effect over the Andes (red box) and exhibits inconsistent artifacts of high pressure (red ellipses). In contrast, the Bottom Row (with constraints) successfully reproduces physically valid states, showing correct wind deceleration induced by topography and removing the spurious pressure anomalies.

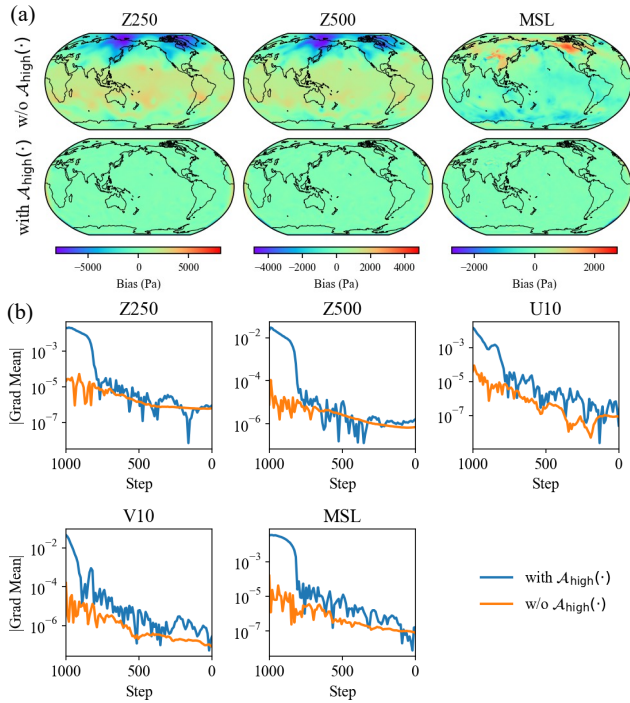


Figure 5. Impact of $\mathcal{A}_{\text{high}}(\cdot)$ operator. (a) Bias distributions. (b) Evolution of gradients during diffusion posterior sampling, illustrating the trajectory from timestep $t = 1000$ to 0 for both methods.

five GCMs. For example, relative to BCSD, ZSSD reduces the MAE from 1.72 to 1.08 on MIROC6. Compared with existing zero-shot approaches (DDRM and vanilla DPS), ZSSD demonstrates consistently stronger generalization, indicating its ability to handle both grid misalignment and distribution shifts between reanalysis data and climate model simulations. These results suggest that ZSSD enables effective cross-domain downscaling from ERA5 to GCMs without model-specific retraining. Due to the poor performance of supervised methods on unpaired tasks, we present

their results in Appendix B.1.

Furthermore, Fig. 3 demonstrates the zero-shot capabilities of ZSSD from both spectral and spatial perspectives. Quantitatively, (a) shows that while raw GCMs (dashed lines) exhibit significant energy loss at high frequencies, ZSSD outputs (solid lines) successfully restore the power spectrum, closely aligning with the ERA5 reference. This spectral consistency translates into realistic spatial reconstructions in (b), where ZSSD successfully recovers coherent vortex structures and detailed textures from the diffuse, coarse inputs. More variables are shown in Appendix B.2

5.3. Ablation Study

Impact of Boundary Conditions on the Prior. To validate the architectural choices of our physics-consistent climate prior, we conduct an ablation study focusing on conditions.

We assess the necessity of conditioning the diffusion process. Fig. 4 compares random samples generated by the prior with and without any conditions. Without conditions, the generated wind fields are overly smooth and exhibit weak interactions with terrain features. In particular, the flow fails to reflect sharp transitions at coastlines or topographically induced constraints. By contrast, conditioning on DEM and LSM yields physically more plausible structures. For example, along the west coast of South America, the model successfully captures sharp gradients at the land-sea interface, and reflects the influence of orographic blocking effects of the Andes. These observations suggest that boundary conditioning is essential for preventing unphysical artifacts and enforcing terrain-aware flow structures.

Impact of $\mathcal{A}_{\text{high}}(\cdot)$ operator. We evaluate the effectiveness of $\mathcal{A}_{\text{high}}(\cdot)$ in mitigating the vanishing gradient problem inherent to low-dimensional spaces, specifically within 5.0° paired tasks utilizing physics-consistent priors. Fig. 5(a) presents a quantitative comparison of bias distributions between the with and without $\mathcal{A}_{\text{high}}(\cdot)$. The without $\mathcal{A}_{\text{high}}(\cdot)$

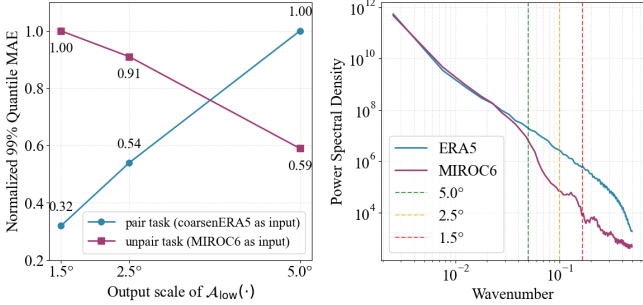


Figure 6. Impact of the output scale of the $\mathcal{A}_{\text{low}}(\cdot)$ operator. (a) The normalized 99% quantile MAE at different output scales (1.5° , 2.5° , and 5.0°). (b) Comparison of PSD between ERA5 and MIROC6. The vertical dashed lines correspond to the wavenumbers for the 5.0° , 2.5° , and 1.5° scales, respectively.

exhibits severe bias, particularly for pressure-related variables, indicating insufficient constraint on the generative process under large scaling factors. In contrast, incorporating $\mathcal{A}_{\text{high}}(\cdot)$ substantially reduces both the magnitude and spread of the bias, resulting in a much lower and more centered bias distribution.

To investigate the underlying cause of this performance gap, we analyze the evolution of guidance gradients throughout the diffusion sampling process in Fig. 5(b). We observe a critical disparity: the without $\mathcal{A}_{\text{high}}(\cdot)$ suffers from a vanishing gradient problem, where the gradient magnitude remains consistently small and sluggish throughout the denoising steps ($t = 1000 \rightarrow 0$). This weak signal fails to provide sufficient direction, preventing the posterior from converging to the ground truth. Conversely, with $\mathcal{A}_{\text{high}}(\cdot)$ maintains gradients with larger magnitude and temporal variation, enabling effective guidance during posterior sampling and facilitating convergence toward physical consistency.

Impact of $\mathcal{A}_{\text{low}}(\cdot)$ operator. Building on the mitigation of the vanishing gradient problem, we further analyze the role of the output scale of the low-resolution operator $\mathcal{A}_{\text{low}}(\cdot)$ under paired and unpaired evaluation settings. We observe markedly different sensitivities across the two tasks. As shown in Fig. 6(a), the normalized 99% quantile MAE in the paired task increases with the output scale of $\mathcal{A}_{\text{low}}(\cdot)$. By contrast, in the unpaired setting using MIROC6 inputs, the reconstruction error decreases substantially as the output scale increases.

Inspired by studies on spectral inconsistencies between climate models and reanalysis data (Hess et al., 2025), we attribute this behavior to mesoscale spectral mismatch between GCMs and ERA5. As illustrated in Fig. 6(b), the Power Spectral Density (PSD) of MIROC6 diverges significantly from the ERA5 reference in the frequency domain, particularly at scales finer than 5° (corresponding to higher wavenumbers), while the large-scale components remain

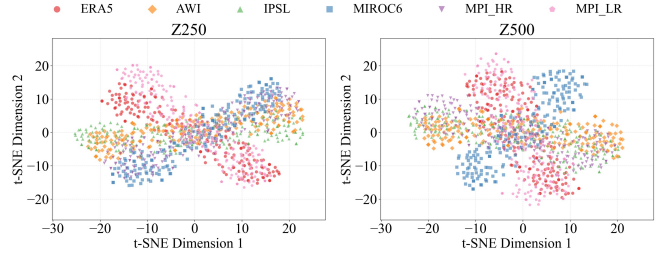


Figure 7. t-SNE visualization of U10 and V10 fields across ERA5 and various climate models.

relatively consistent.

We hypothesize that when $\mathcal{A}_{\text{low}}(\cdot)$ operates at a smaller output scale, it retains these mismatched high-frequency components. Consequently, the subsequent posterior sampling inherits these spectral discrepancies, leading to higher errors. In contrast, when the output scale exceeds approximately 5° , $\mathcal{A}_{\text{low}}(\cdot)$ effectively suppresses inconsistent mesoscale components while retaining coherent large-scale structure. Conditioning on this filtered representation allows posterior sampling to focus on physically consistent information, thereby reducing error in the unpaired setting.

5.4. Case Study

t-SNE visualization among ERA5 and GCMs. Fig 7 visualizes 100 random samples each from ERA5 and five GCMs using t-SNE. The distinct clustering in Z250 and Z500 reveals a significant domain gap between ERA5 and the GCMs. This distribution shift explains the performance degradation of the supervised model observed in Appendix B.1 when directly transferring supervised models. Furthermore, it validates the necessity of using $\mathcal{A}_{\text{low}}(\cdot)$ in ZSSD to align the raw data. More variables are shown in Appendix B.3.

6. Conclusion

We presented Zero-Shot Statistical Downscaling (ZSSD), a zero-shot generative framework designed to downscale the coarse outputs of GCMs to a high-resolution scale without paired data in training. By integrating a Physics-Consistent Climate Prior with a Unified Coordinate Guidance strategy, ZSSD effectively overcomes the physical inconsistencies and vanishing gradient issues inherent in vanilla DPS, particularly under large scaling factors. Extensive experiments demonstrate that our approach achieves SOTA 99th percentile bias correction performance on unpaired benchmarks, successfully recovering details in weather events like tropical cyclones. Although the generative speed of ZSSD is relatively slow due to the multiple inference steps, it offers a robust and scalable solution for climate risk assessment in

future warming scenarios.

Software and Data

We will make all code publicly available upon acceptance.

Impact Statement

This paper presents work whose goal is to advance the field of Machine Learning. The potential societal consequences of our work are positive, as it provides a scalable solution for assessing regional climate risks and extreme weather events, such as tropical cyclones. By bridging the gap between coarse global simulations and local impacts, this research supports better-informed decision-making for disaster preparedness and climate adaptation strategies under future warming scenarios. There are no potential negative societal consequences that we feel must be specifically highlighted here.

References

Boucher, O., Servonnat, J., Albright, A. L., Aumont, O., Balkanski, Y., Bastrikov, V., Bekki, S., Bonnet, R., Bony, S., Bopp, L., et al. Presentation and evaluation of the ipsl-cm6a-lr climate model. *Journal of Advances in Modeling Earth Systems*, 12(7):e2019MS002010, 2020.

Calvin, K., Dasgupta, D., Krinner, G., Mukherji, A., Thorne, P. W., Trisos, C., Romero, J., Aldunce, P., Barret, K., Blanco, G., et al. Ipc, 2023: Climate change 2023: Synthesis report, summary for policy-makers. contribution of working groups i, ii and iii to the sixth assessment report of the intergovernmental panel on climate change [core writing team, h. lee and j. romero (eds.)]. ipcc, geneva, switzerland. *IPCC, 2023: Climate Change 2023: Synthesis Report. Contribution of Working Groups I, II and III to the Sixth Assessment Report of the Intergovernmental Panel on Climate Change [Core Writing Team, H. Lee and J. Romero (eds.)]*. IPCC, Geneva, Switzerland., pp. 1–34, 2023.

Chung, H., Kim, J., Mccann, M. T., Klasky, M. L., and Ye, J. C. Diffusion posterior sampling for general noisy inverse problems. *arXiv preprint arXiv:2209.14687*, 2022a.

Chung, H., Sim, B., Ryu, D., and Ye, J. C. Improving diffusion models for inverse problems using manifold constraints. *Advances in Neural Information Processing Systems*, 35:25683–25696, 2022b.

Efron, B. Tweedie’s formula and selection bias. *Journal of the American Statistical Association*, 106(496):1602–1614, 2011.

Eyring, V., Bony, S., Meehl, G. A., Senior, C. A., Stevens, B., Stouffer, R. J., and Taylor, K. E. Overview of the coupled model intercomparison project phase 6 (cmip6) experimental design and organization. *Geoscientific Model Development*, 9(5):1937–1958, 2016.

Gao, X., Sitharam, M., and Roitberg, A. E. Bounds on the jensen gap, and implications for mean-concentrated distributions. *arXiv preprint arXiv:1712.05267*, 2017.

Groenke, B., Madaus, L., and Monteleoni, C. Climalign: Unsupervised statistical downscaling of climate variables via normalizing flows. In *Proceedings of the 10th International Conference on Climate Informatics*, pp. 60–66, 2020.

Gupta, A. and Nagar, D. *Matrix Variate Distributions*, volume 104. CRC Press, 1999.

Hersbach, H., Bell, B., Berrisford, P., Bivat, G., Horányi, A., Muñoz Sabater, J., Nicolas, J., Peubey, C., Radu, R., Rozum, I., et al. Era5 hourly data on pressure levels from 1940 to present. *Copernicus climate change service (c3s) climate data store (cds)*, 10:24381, 2023.

Hess, P., Aich, M., Pan, B., and Boers, N. Fast, scale-adaptive and uncertainty-aware downscaling of earth system model fields with generative machine learning. *Nature Machine Intelligence*, pp. 1–11, 2025.

Hewitson, B. C. and Crane, R. G. Climate downscaling: techniques and application. *Climate Research*, 7(2):85–95, 1996.

Ho, J., Jain, A., and Abbeel, P. Denoising diffusion probabilistic models. In Larochelle, H., Ranzato, M., Hadsell, R., Balcan, M., and Lin, H. (eds.), *Advances in Neural Information Processing Systems*, volume 33, pp. 6840–6851. Curran Associates, Inc., 2020.

Kawar, B., Elad, M., Ermon, S., and Song, J. Denoising diffusion restoration models. *Advances in neural information processing systems*, 35:23593–23606, 2022.

Kim, K. and Ye, J. C. Noise2score: Tweedie’s approach to self-supervised image denoising without clean images. In Ranzato, M., Beygelzimer, A., Dauphin, Y., Liang, P., and Vaughan, J. W. (eds.), *Advances in Neural Information Processing Systems*, volume 34, pp. 864–874. Curran Associates, Inc., 2021.

Langley, P. Crafting papers on machine learning. In Langley, P. (ed.), *Proceedings of the 17th International Conference on Machine Learning (ICML 2000)*, pp. 1207–1216, Stanford, CA, 2000. Morgan Kaufmann.

Li, H., Wang, Y., Huang, G., Tao, W., and Lin, P. Generative Downscaling and Bias Correction of Multivariable

Earth System Model Simulations. *Geophysical Research Letters*, 52(18):e2025GL117397, September 2025. ISSN 0094-8276, 1944-8007.

Liang, J., Cao, J., Sun, G., Zhang, K., Van Gool, L., and Timofte, R. Swinir: Image restoration using swin transformer. In *Proceedings of the IEEE/CVF international conference on computer vision*, pp. 1833–1844, 2021.

Mardani, M., Song, J., Kautz, J., and Vahdat, A. A variational perspective on solving inverse problems with diffusion models. *arXiv preprint arXiv:2305.04391*, 2023.

Mardani, M., Brenowitz, N., Cohen, Y., Pathak, J., Chen, C.-Y., Liu, C.-C., Vahdat, A., Nabian, M. A., Ge, T., Subramaniam, A., et al. Residual corrective diffusion modeling for km-scale atmospheric downscaling. *Communications Earth & Environment*, 6(1):124, 2025.

Mauritsen, T., Bader, J., Becker, T., Behrens, J., Bittner, M., Brokopf, R., Brovkin, V., Claussen, M., Crueger, T., Esch, M., et al. Developments in the mpi-m earth system model version 1.2 (mpi-esm1.2) and its response to increasing co2. *Journal of Advances in Modeling Earth Systems*, 11(4):998–1038, 2019.

Mayer, L., Jakobsson, M., Allen, G., Dorschel, B., Falconer, R., Ferrini, V., Lamarche, G., Snaith, H., and Weatherall, P. The nippon foundation—gebco seabed 2030 project: The quest to see the world’s oceans completely mapped by 2030. *Geosciences*, 8(2):63, 2018.

Meehl, G. A., Boer, G. J., Covey, C., Latif, M., and Stouffer, R. J. The coupled model intercomparison project (cmip). *Bulletin of the American Meteorological Society*, 81(2): 313–318, 2000.

O’Neill, B. C., Tebaldi, C., Van Vuuren, D. P., Eyring, V., Friedlingstein, P., Hurtt, G., Knutti, R., Kriegler, E., Lamarque, J.-F., Lowe, J., et al. The scenario model intercomparison project (scenariomip) for cmip6. *Geoscientific Model Development*, 9(9):3461–3482, 2016.

Schmidt, J., Schmidt, L., Strnad, F. M., Ludwig, N., and Hennig, P. A generative framework for probabilistic, spatiotemporally coherent downscaling of climate simulation. *npj Climate and Atmospheric Science*, 8(1):270, 2025.

Semmler, T., Danilov, S., Gierz, P., Goessling, H. F., Hegewald, J., Hinrichs, C., Koldunov, N., Khosravi, N., Mu, L., Rackow, T., et al. Simulations for cmip6 with the awi climate model awi-cm-1-1. *Journal of Advances in Modeling Earth Systems*, 12(9):e2019MS002009, 2020.

Simic, S. On a global upper bound for jensen’s inequality. *Journal of Mathematical Analysis and Applications*, 343(1):414–419, 2008. ISSN 0022-247X.

Tatebe, H., Ogura, T., Nitta, T., Komuro, Y., Ogochi, K., Takemura, T., Sudo, K., Sekiguchi, M., Abe, M., Saito, F., et al. Description and basic evaluation of simulated mean state, internal variability, and climate sensitivity in miroc6. *Geoscientific Model Development*, 12(7):2727–2765, 2019.

Tie, R., Zhong, X., Shi, Z., Li, H., Chen, B., Liu, J., and Libo, W. Generative artificial intelligence improves projections of climate extremes. *arXiv preprint arXiv:2508.16396*, 2025.

Vincent, P. A connection between score matching and denoising autoencoders. *Neural Computation*, 23(7):1661–1674, 2011.

Wang, X., Yu, K., Wu, S., Gu, J., Liu, Y., Dong, C., Qiao, Y., and Change Loy, C. Esrgan: Enhanced super-resolution generative adversarial networks. In *Proceedings of the European conference on computer vision (ECCV) workshops*, pp. 0–0, 2018.

Wang, Y., Yu, J., and Zhang, J. Zero-shot image restoration using denoising diffusion null-space model. *arXiv preprint arXiv:2212.00490*, 2022.

Wood, A. W., Maurer, E. P., Kumar, A., and Lettenmaier, D. P. Long-range experimental hydrologic forecasting for the eastern united states. *Journal of Geophysical Research: Atmospheres*, 107(D20):ACL–6, 2002.

Zhu, Y., Zhang, K., Liang, J., Cao, J., Wen, B., Timofte, R., and Van Gool, L. Denoising diffusion models for plug-and-play image restoration. In *Proceedings of the IEEE/CVF conference on computer vision and pattern recognition*, pp. 1219–1229, 2023.

A. Supplementary Methods

A.1. Supplementary Methods in Section 4.2

From the noisy state \mathbf{X}_t using Tweedie's formula (Kim & Ye, 2021; Efron, 2011) we have the posterior mean:

$$\hat{X}_0(\mathbf{X}_t, \mathbf{C}) := \mathbb{E}[\mathbf{X}_0 | \mathbf{X}_t, \mathbf{C}] = \frac{\mathbf{X}_t - \sqrt{1 - \bar{\alpha}_t} \epsilon_\theta(\mathbf{X}_t, t, \mathbf{C})}{\sqrt{\bar{\alpha}_t}}. \quad (7)$$

However, using only Eq. (7) for climate downscaling will result in inconsistencies with low resolution observations and other issues. Therefore, posterior sampling based on Bayes' rule is required. we have:

$$\log p(\mathbf{X}_t | \mathbf{Y}, \mathbf{C}) \propto \log p(\mathbf{X}_t | \mathbf{C}) + \log p(\mathbf{Y} | \mathbf{X}_t, \mathbf{C}). \quad (8)$$

Taking the gradient with respect to \mathbf{X}_t to obtain the conditional score function:

$$\nabla_{\mathbf{X}_t} \log p(\mathbf{X}_t | \mathbf{Y}, \mathbf{C}) = \nabla_{\mathbf{X}_t} \log p(\mathbf{X}_t | \mathbf{C}) + \nabla_{\mathbf{X}_t} \log p(\mathbf{Y} | \mathbf{X}_t, \mathbf{C}). \quad (9)$$

In the framework of diffusion models, the noise-prediction network $\epsilon_\theta(\mathbf{X}_t, t)$ is essentially equivalent to the time-dependent score function $\nabla_{\mathbf{X}_t} \log p(\mathbf{X}_t)$ (Vincent, 2011). Therefore, once ϵ_{θ^*} is acquired by minimizing in Eq. (4), we can use the approximation $\nabla_{\mathbf{X}_t} \log p(\mathbf{X}_t | \mathbf{C}) \simeq -\epsilon_{\theta^*}(X_t, t, \mathbf{C})/\sqrt{1 - \bar{\alpha}_t}$, and the approximation error arises from an optimization error with respect to Eq. (4).

The second term $\nabla_{\mathbf{X}_t} \log p(\mathbf{Y} | \mathbf{X}_t, \mathbf{C})$ in Eq. (9) is intractable, but according to $p(\mathbf{Y} | \mathbf{X}_t, \mathbf{C}) = \mathbb{E}_{\mathbf{X}_0 \sim p(\mathbf{X}_0 | \mathbf{X}_t, \mathbf{C})} [p(\mathbf{Y} | \mathbf{X}_0)]$ and $\hat{\mathbf{X}}_0 := \mathbb{E}[\mathbf{X}_0 | \mathbf{X}_t, \mathbf{C}] = \mathbb{E}_{\mathbf{X}_0 \sim p(\mathbf{X}_0 | \mathbf{X}_t, \mathbf{C})} [\mathbf{X}_0]$, it can be approximated by conditioning on the estimated clean image $\hat{\mathbf{X}}_0$:

$$p(\mathbf{Y} | \mathbf{X}_t, \mathbf{C}) \simeq p(\mathbf{Y} | \hat{\mathbf{X}}_0(\mathbf{X}_t, \mathbf{C})), \quad (10)$$

implying that the outer expectation of $p(\mathbf{Y} | \mathbf{X}_0)$ over the posterior distribution is replaced with the inner expectation of \mathbf{X}_0 , so the approximation error in Eq. (10) can be quantified with the Jensen gap (Gao et al., 2017; Simic, 2008). Furthermore, this Jensen's gap has an exact upper bound under our inverse problem subject to Gaussian noise (Chung et al., 2022a).

A.2. Supplementary Evaluation Methods

We define the MAE and RMSE at the 99th percentile as follows:

$$\text{MAE} = \frac{1}{W \sum_{j=1}^H w_j} \sum_{i=1}^W \sum_{j=1}^H w_j |Q_{\text{model},i,j} - Q_{\text{ERA5},i,j}|, \quad (11)$$

$$\text{RMSE} = \sqrt{\frac{1}{W \sum_{j=1}^H w_j} \sum_{i=1}^W \sum_{j=1}^H w_j (Q_{\text{model},i,j} - Q_{\text{ERA5},i,j})^2}, \quad (12)$$

where $W = 1440$ and $H = 720$ denote the number of grid points in the longitude and latitude directions, respectively. $Q_{\text{model},i,j}$ and $Q_{\text{ERA5},i,j}$ represent the 99th percentile values at grid point (i, j) . Crucially, $w_j = \cos(\phi_j)$ represents the latitude weight, which corrects for the area distortion inherent in the spherical geometry of the Earth.

B. Supplementary Results

B.1. Supplementary Results in Supervised-based Methods

Table 3 shows that supervised methods excel in the Paired Task, benefiting from direct learning on paired data, with CorrDiff achieving the best performance. However, when directly transferred to the Unpaired Task (IPSL), their performance deteriorates significantly due to domain shifts, yielding results even inferior to the coarse input. In contrast, while our ZSSD shows slightly higher errors than supervised baselines on paired data, it remains within an acceptable range. More importantly, ZSSD demonstrates superior generalization, significantly outperforming supervised methods in the challenging unpaired scenario.

Table 3. Quantitative results of supervised downscaling methods.

METHOD	PAIRED TASK (SYNTHETIC)			UNPAIRED TASK (REAL GCMs)	
	1.5° ($\times 6$)	2.5° ($\times 10$)	5.0° ($\times 20$)	IPSL	
SWINIR	0.08 / 0.16	0.15 / 0.27	0.32 / 0.50		1.32 / 2.10
ESRGAN	0.07 / 0.16	0.13 / 0.25	0.29 / 0.44		<u>1.18 / 1.83</u>
CORRDIFF	0.07 / 0.15	0.13 / 0.25	0.28 / 0.45		1.16 / 1.79

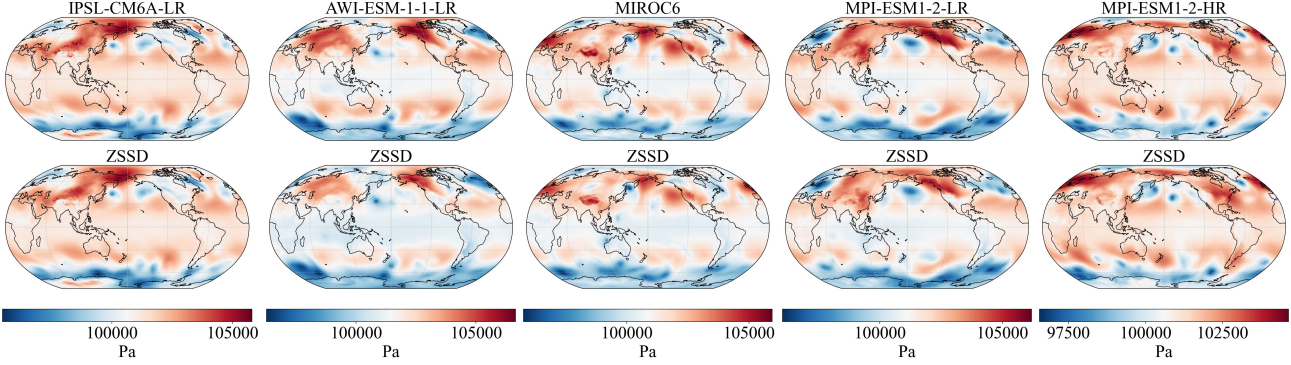


Figure 8. Visualization of MSL fields across different GCMs before and after downscaling. The time period is consistent with Fig. 3. Note that unlike surface pressure, which mirrors rugged topography, MSL is a derived variable designed to filter out orographic effects, resulting in a naturally smoother field at synoptic scales, although major features like the Tibetan Plateau and the Andes remain visually discernible. To quantify the variations that are less apparent, we provide a spectral analysis in Fig. 11 to illustrate the differences in small-scale energy.

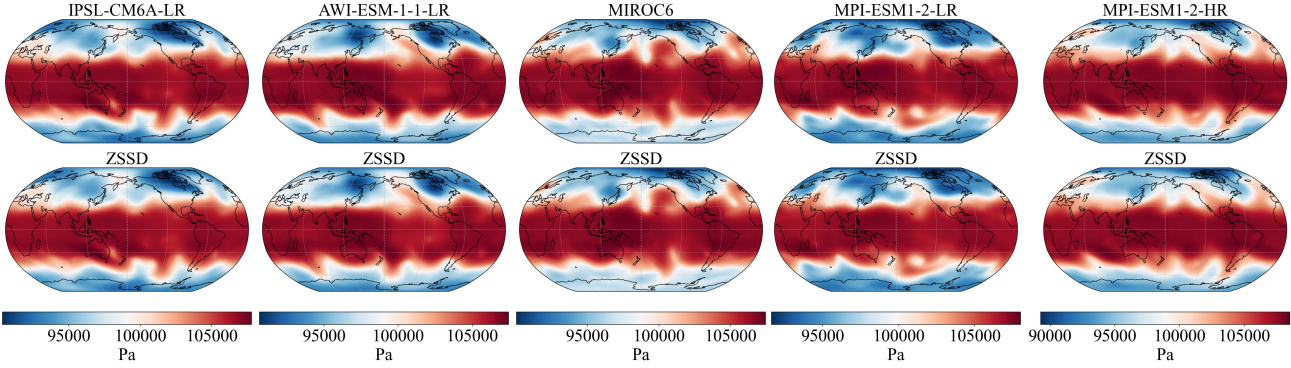


Figure 9. Visualization of Z250 fields across different GCMs before and after downscaling. The time period is consistent with Fig. 3. Since upper-level fields are generally smooth, making differences in small-scale details difficult to distinguish visually, we conducted a spectral analysis in Fig. 11.

B.2. Supplementary Results in main results

This section complements Fig. 3 by further illustrating the downscaling results for pressure-related variables. Since upper-level fields are generally smooth, the visual differences before and after downscaling are not significant for Z250 and Z500 (see Fig. 9 and Fig. 10). In contrast, MSL shows clear improvements in detail over regions like the Tibetan Plateau and the Andes (see Fig. 8). To capture nuances beyond visual inspection, we further analyzed the spectral characteristics (Fig. 11). In the frequency domain, distinct behaviors emerge at small scales: for MSL, GCMs tend to overestimate high-frequency energy, whereas our results align consistently with ERA5. Conversely, for Z250 and Z500, where the small-scale energy in GCMs nearly vanishes, our method effectively recovers these high-frequency components, exhibiting slightly higher energy levels than ERA5. Despite the limited visual change, it is important to note that Z250 and Z500 remain crucial for the accurate localization and identification of TCs.

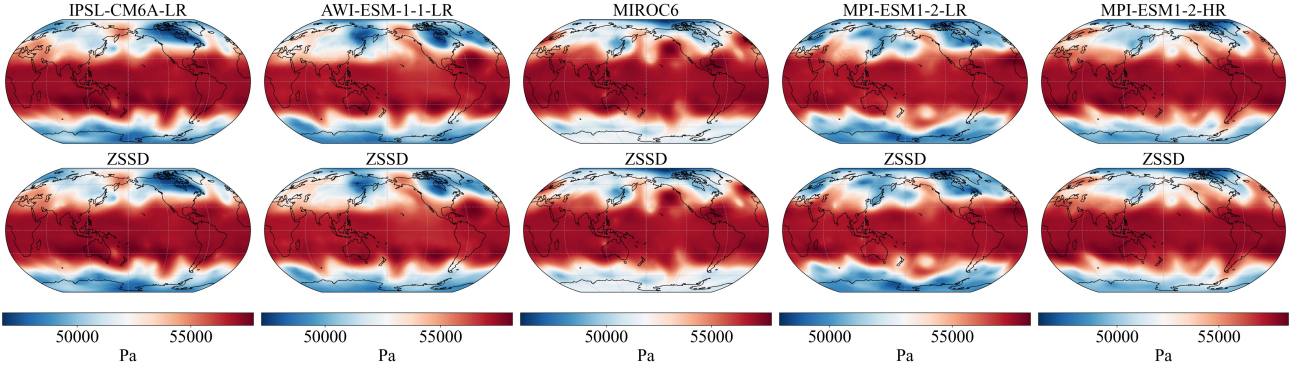


Figure 10. Visualization of Z500 fields across different GCMs before and after downscaling. The time period is consistent with Fig. 3. Since upper-level fields are generally smooth, making differences in small-scale details difficult to distinguish visually, we conducted a spectral analysis in Fig. 11.

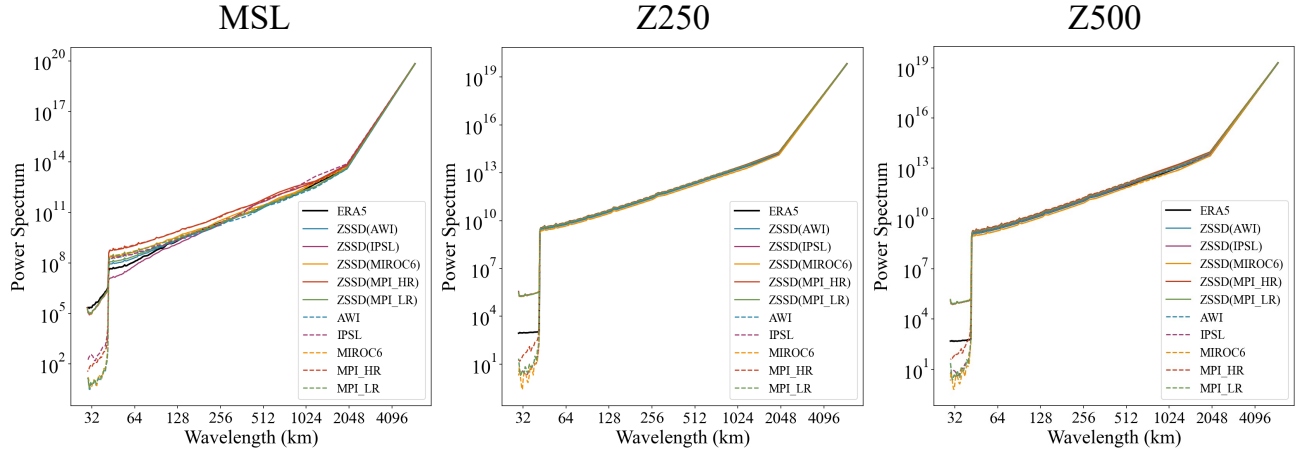


Figure 11. PSD of MSL, Z250, Z500 fields across different GCMs before and after downscaling. The time period is consistent with Fig. 3.

B.3. Supplementary Results in case study

As shown in Fig. 12, a significant domain gap still exists between ERA5 and GCMs for U10, V10, and MSL.

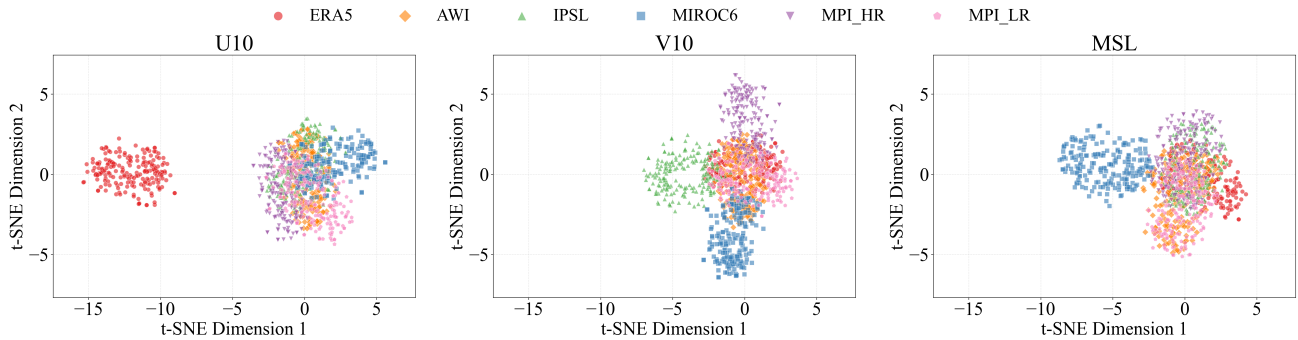


Figure 12. t-SNE visualization of U10, V10 and MSL fields across ERA5 and various climate models.